



Pergamon

Acta mater. 49 (2001) 2723–2737



www.elsevier.com/locate/actamat

N-SITE MODELING OF A 3D VISCOPLASTIC POLYCRYSTAL USING FAST FOURIER TRANSFORM

R. A. LEBENSOHN

Instituto de Física Rosario (UNR-CONICET), 27 de Febrero 210 Bis, 2000 Rosario, Argentina

(Received 7 November 2000; received in revised form 18 April 2001; accepted 18 April 2001)

Abstract—We present a formulation to compute the local response of elastic and viscoplastic anisotropic 3D polycrystals based on the Fast Fourier Transform (FFT) algorithm. This formulation is conceived for periodic heterogeneous microstructures and also for materials with random spatial distribution of heterogeneities. The approach is of the n -site kind, provides an exact solution of the equilibrium equation and has better numerical performance than small-scale FEM. The viscoplastic FFT formulation combined with an ad-hoc microstructure updating scheme is used to predict local states, morphology and texture evolution of ideal f.c.c. polycrystals. The model predicts strain localization, intragranular misorientation and subgrain formation and overall textures which are smoother than those obtained with classical 1-site schemes, in better agreement with experiments. © 2001 Acta Materialia Inc. Published by Elsevier Science Ltd. All rights reserved.

Keywords: Theory & modeling; Polycrystal; Mechanical properties (plastic); Texture; Microstructure

1. INTRODUCTION

This paper is concerned with the determination of local states of heterogeneous materials. Due to the development of new characterization techniques which allow the investigation of the materials properties and structures down to atomic scale and the increasing capability of computers, small-scale mechanisms of deformation and damage are being incorporated into multiscale models of plasticity and fracture. The modeling of, for instance, diffusion-controlled deformation mechanisms or cavitation which are essential to explain phenomena like fatigue, creep or ductile fracture of complex polycrystalline materials, requires realistic predictions of intragranular strain and stress concentrations. The Finite Element method (FEM) at small-scale as well as multisite homogenization models have been used in the past to model the local behavior of complex microstructures. On the one hand, small-scale FEM techniques [1–14] have been used to deal with such complex microstructures when their complexity is due to the contrast of properties between phases [3, 5, 6, 8] and/or the morphology of a large number of inclusions of irregular shape [3, 5, 8] and/or the local directional properties in polycrystals with anisotropic constituent grains [1, 2, 4, 6–14]. However, the difficulties related to meshing and the large number of

degrees of freedom required by such FEM calculations limit the complexity and the size of the microstructures that can be investigated by these methods. On the other hand, the prediction of intracrystalline states using homogenization techniques requires n -site selfconsistent approaches [15, 16] instead of the classical 1-site formulations [17, 18] in which ideal crystals are considered to deform embedded in a homogeneous medium with average properties. The size of the problem which can be solved by means of the n -site selfconsistent formulation is also dramatically limited by the total number of sites involved in the calculation, even in the simplified case of considering only first-neighbor interactions [15, 16].

The aforementioned limitations of both the small-scale FEM and the n -site selfconsistent models can be overcome with a novel approach, based on the FFT algorithm. Moulinec and Suquet [19, 20] and Michel *et al.* [21, 22] recently developed a method based on FFT to compute the overall linear (elastic [19–21]) and non-linear (elastoplastic [19, 20] and viscoplastic [21, 22]) response of composites consisting of two isotropic phases with different properties. The main characteristics of the FFT approach are:

- (a) The method is based on the solution of a cell problem for a representative volume element (RVE) with periodic boundary conditions. In this way, it is implicitly assumed that the size of the heterogeneities is small compared with the specimen

E-mail address: lebenso@lanl.gov (R. A. Lebensohn)

dimensions. For actual periodic microstructures the size and properties of the RVE are naturally specified from the properties of a unit cell which generates the whole microstructure by periodic repetition. For spatially random microstructures, the RVE should be chosen to be statistically representative of the whole microstructure.

- (b) The formulation is of the n -site kind with no cut-off distance for the interaction. In other words, the interaction of one site of the discretized RVE with all the other sites is taken into account. Consequently, this formulation does not involve any homogenization assumption and—for an infinitely refined discretization of the RVE—it would provide an exact solution of the equilibrium equation.

Although, until now, the main interest of Suquet and coworkers [19–22] has been to calculate the overall behavior of two-phase isotropic composites, the FFT method can also be used to obtain the local response of anisotropic polycrystals in which the source of heterogeneity is the existence of grains with directional properties and different crystallographic orientations. In the present work, the elastic FFT formulation is applied to obtain the local response of an ideal 3D polycrystal. This elastic case will serve us to introduce the FFT formulation for viscoplastic polycrystals deforming by dislocation glide. The plan of the paper is as follows: in Section 2 we describe the kind of model polycrystal we use and its corresponding discretization. In Section 3 we review the elastic FFT formulation and algorithm and compare n -site FFT results with 1-site selfconsistent predictions for the same model polycrystal. In Section 4 we present the extension of the FFT model to the viscoplastic regime. To start with, the formulation, the ad-hoc criterion for microstructure updating and the algorithm are presented. As in the elastic case, the local states predicted with the n -site FFT and the 1-site selfconsistent models are compared. Next, a detailed study of the convergence of the method is presented. The section is closed with two illustrative applications of the viscoplastic FFT formulation for the prediction of morphology and texture evolution in f.c.c. polycrystals and a discussion about the numerical performance of the method.

2. DISCRETIZATION

In what follows we will work with idealized 3D polycrystals, initially consisting of prismatic grains arranged in a regular fashion, rather than use other available schemes [15, 23] to generate microstructures which may look more realistic but are more complicated to analyze. Figure 1 shows a schematic representation of such ideal 3D polycrystal and its discretization. The polycrystal (i.e. the RVE) consists of 512 prismatic grains arranged in a $8 \times 8 \times 8$ structure. Due to the requirement of periodic boundary conditions, this structure should be periodically repeated

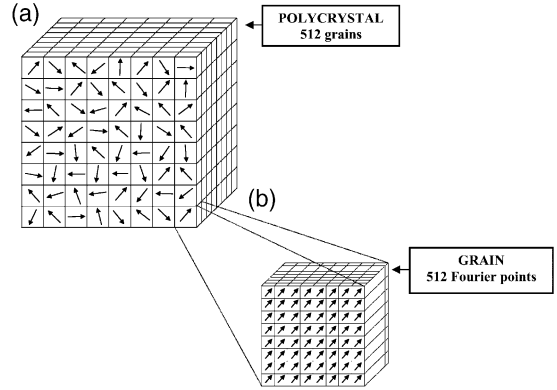


Fig. 1. Schematic representation of the initial discretization of a 3D polycrystal. (a) The polycrystal consists of 512 cubic grains arranged in a $8 \times 8 \times 8$ structure. Arrows pointing in different directions indicate different orientations of each crystallite. (b) Each grain is discretized into 512 cubes arranged in a $8 \times 8 \times 8$ structure. The points of the Fourier grid are located in the center of each cube. Arrows pointing in the same direction indicate that for a given grain the initial orientations associated with the Fourier points are identical. The entire Fourier grid consists of $64 \times 64 \times 64$ points.

along the three spatial directions. In Fig. 1(a), the arrows pointing in different directions indicate different orientations of each crystallite. Each grain, in turn, is subdivided into 512 prisms arranged in a $8 \times 8 \times 8$ structure [Fig. 1(b)] with the points of the Fourier grid placed in the center of each prism. The arrows pointing in the same direction indicate that, for a given grain, the initial orientations associated with each Fourier point are identical. In the case of the figure, the entire Fourier grid has $64 \times 64 \times 64$ points. Throughout this work, in order to study the influence of the spatial resolution, we will also discretize the same $8 \times 8 \times 8$ -grain structure using other grids, such as a coarser $32 \times 32 \times 32$ grid (64 points per grain) and a more refined $128 \times 128 \times 128$ grid (4096 points per grain). The formal definition of the 3D Fourier grid $\{\mathbf{x}_d\}$ in real space is given by:

$$\{\mathbf{x}_d\} = \left\{ \left((i_1 - 1) \frac{L_1}{N_1}, (i_2 - 1) \frac{L_2}{N_2}, (i_3 - 1) \frac{L_3}{N_3} \right); \quad (1) \right. \\ \left. i_k = 1, \dots, N_k, k = 1, 3 \right\}$$

where L_k and N_k are the length (i.e. the period) and the number of Fourier points in each x_k -direction. Particularly in the case of the figure (for equiaxed grains and RVE) we have: $L_1 = L_2 = L_3$ and $N_1 = N_2 = N_3 = 64$.

3. ELASTIC CASE

3.1. Formulation

Following the general framework established by Moulinec and Suquet [19, 20], we present here the

solution of the local problem of an inhomogeneous elastic medium undergoing an applied strain E_{ij} . The local problem for a heterogeneous RVE with periodic boundary conditions is written as:

$$\begin{cases} \sigma(\mathbf{x}) = C(\mathbf{x}) : \varepsilon(\mathbf{x}) & \text{in RVE} & (2a) \\ \sigma_{ij,j} = 0 & \text{in RVE} & (2b) \\ \text{periodic boundary conditions} & \text{across RVE} & (2c) \end{cases}$$

where $\varepsilon(\mathbf{x})$ and $\sigma(\mathbf{x})$ are the local strain and stress fields induced in the material and $C(\mathbf{x})$ is the local elastic stiffness. Defining a homogeneous reference medium of stiffness C° , system (2) is formally equivalent to:

$$\begin{cases} \sigma(\mathbf{x}) = C^\circ : \varepsilon(\mathbf{x}) + \tau(\mathbf{x}) & \text{in RVE} & (3a) \\ \sigma_{ij,j} = 0 & \text{in RVE} & (3b) \\ \text{periodic boundary conditions} & \text{across RVE} & (3c) \end{cases}$$

where the perturbation field associated with the heterogeneity is given by:

$$\tau(\mathbf{x}) = \delta C(\mathbf{x}) : \varepsilon(\mathbf{x}) \quad (4)$$

with $\delta C(\mathbf{x}) = C(\mathbf{x}) - C^\circ$. Combining the constitutive equation (3a) and the equilibrium equation (3b) we get:

$$C_{ijkl}^\circ u_{k,lj}(\mathbf{x}) + \tau_{ij,j}(\mathbf{x}) = 0 \quad (5)$$

where $u_k(\mathbf{x})$ is the periodic displacement vector field. The term $\tau_{ij,j}(\mathbf{x})$ can be thought as a fictitious body force field applied to the RVE. Solving (5) by means of the Green function method gives [24]:

$$C_{ijkl}^\circ G_{km,lj}(\mathbf{x} - \mathbf{x}') + \delta_{im} \delta(\mathbf{x} - \mathbf{x}') = 0 \quad (6)$$

where the Green function $G_{km}(\mathbf{x} - \mathbf{x}')$ is the displacement component in the x_k -direction at the point \mathbf{x} when a unit force is applied in the x_m -direction at the point \mathbf{x}' of the RVE. The local fluctuation of the displacement field can be obtained as:

$$\tilde{u}_k(\mathbf{x}) = \int_{R^3} G_{ki}(\mathbf{x} - \mathbf{x}') \tau_{ij,j}(\mathbf{x}') \, d\mathbf{x}' \quad (7)$$

After integrating by parts, deriving and symmetrizing, the local strain fluctuation $\tilde{\varepsilon} = \varepsilon - E$ can be expressed as a convolution in real space:

$$\tilde{\varepsilon}_{ij}(\mathbf{x}) = \text{sym} \left(\int_{R^3} G_{ik,jl}(\mathbf{x} - \mathbf{x}') \tau_{kl}(\mathbf{x}') \, d\mathbf{x}' \right). \quad (8)$$

Calling $\Gamma_{ijkl} = \text{sym}(G_{ik,jl})$ and using the symbol of convolution «*», we obtain:

$$\tilde{\varepsilon} = \Gamma_{ijkl} * \tau_{kl}. \quad (9)$$

If (9) is transformed into the Fourier space, it gives a (tensor) product:

$$\hat{\tilde{\varepsilon}}_{ij} = \hat{\Gamma}_{ijkl} \hat{\tau}_{kl} \quad (10)$$

$\hat{\Gamma}_{ijkl}$ can be calculated taking Fourier transform to (6) to obtain:

$$C_{ijkl}^\circ \xi_l \xi_j \hat{G}_{km} = \delta_{im} \quad (11)$$

where ξ is a point of the Fourier space or *frequency*. It follows that:

$$\hat{G}_{ik} = A_{ik}'^{-1} = [\xi_l \xi_j C_{ijkl}^\circ]^{-1} \quad (12)$$

and:

$$\hat{\Gamma}_{ijkl} = -\frac{1}{2} (\xi_l \xi_j A_{ik}'^{-1} + \xi_l \xi_i A_{jk}'^{-1}). \quad (13)$$

With equations (11)–(13), $\hat{\Gamma}_{ijkl}$ can be calculated at any frequency except in the origin of Fourier space (i.e. $\xi = \bar{0}$) where the value of $\hat{\tilde{\varepsilon}}_{ij}$ is given directly by $\hat{\tilde{\varepsilon}}_{ij}|_{\xi=\bar{0}}$ (i.e. the mean value of the strain deviation field in the real space vanishes). The aforementioned boundary condition in Fourier space together with equations (10) and (11)–(13) can be used to obtain the local strain field if the transformed perturbation field $\hat{\tau}_{ij}$ is known. However, the perturbation field in real space $\tau_{ij}(\mathbf{x})$ is not a priori known since it is precisely a function of the unknown local strain [see equation (4)]. Therefore, the problem must be solved iteratively, assuming an initial guess for $\tilde{\varepsilon}_{ij}(\mathbf{x})$ and adopting an appropriate convergence criterion. As stated in [19, 20], the convergence of the method should be related to the fulfillment of the equilibrium condition (2b). To check this condition it is advisable to work in Fourier space rather than in real space since a divergence in the latter is transformed into a contracted product in the former. Hence, the Fourier transform of equation (2b) leads to the following convergence criterion:

$$\frac{\langle |\xi_j \hat{\sigma}_{ij}| \rangle}{\|\hat{\sigma}(\xi = \bar{0})\|} < \delta \quad (14)$$

where $\langle \cdot \rangle$ denotes average over the whole Fourier grid, δ is a small positive constant (typically 10^{-4}) and $\|\hat{\sigma}(\xi = \bar{0})\|$ is an appropriate normalization factor [19, 20].

3.2. Algorithm

The numerical implementation of the previous formulation needs an appropriate discretization [e.g. $\{\mathbf{x}_d\}$ given by equation (1)] in order to allow the application of FFT each time a Fourier transform is required. The algorithm can be initialized with: $\hat{\varepsilon}^0(\mathbf{x}) = 0$ and $\sigma^0(\mathbf{x}) = C^0:E; \forall \mathbf{x} \in \{\mathbf{x}_d\}$. Iteration $(i + 1)$ —provided $\hat{\varepsilon}^i, \sigma^i$ are known—consists of:

1. $\hat{\sigma}^i = \text{fft}(\sigma^i)$
2. Convergence test [equation (14)]: is equilibrium fulfilled? If yes, stop.
3. $\tau^i(\mathbf{x}_d) = \sigma^i(\mathbf{x}_d) - C^0:\hat{\varepsilon}^i(\mathbf{x}_d)$
4. $\hat{\tau}^i = \text{fft}(\tau^i)$
5. For each frequency ξ , calculate $\hat{\Gamma}$ using equations (12) and (13).
6. $\hat{\varepsilon}^{i+1} = \hat{\Gamma}:\hat{\tau}^i$ with $\hat{\varepsilon}^{i+1}|_{\xi=\bar{0}} = 0$
7. $\tilde{\varepsilon}^{i+1} = \text{fft}^{-1}(\hat{\varepsilon}^{i+1})$ and $\sigma^{i+1}(\mathbf{x}_d) = C(\mathbf{x}_d):(E + \tilde{\varepsilon}^{i+1}(\mathbf{x}_d))$
8. Start iteration $(i + 1)$ from step 1.

Here fft and fft^{-1} denote the application of direct and inverse discrete Fast Fourier Transform algorithms (for details see [25], for example), respectively.

3.3. Results

Since the elastic FFT model is presented here just as an introduction to the viscoplastic formulation, we will briefly illustrate the former with predictions of elastic strain heterogeneity in Cu polycrystals and then move forward to the viscoplastic FFT model, leaving other applications of the elastic polycrystal model for future contributions. Figure 2 shows a comparison between the relative longitudinal strain deviation predicted with the n -site elastic FFT formulation

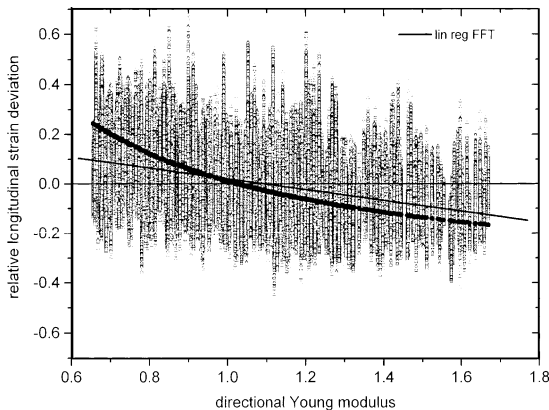


Fig. 2. Relative longitudinal strain deviation calculated with 1-site ELSC and elastic FFT vs directional Young modulus for a Cu polycrystal under axisymmetric deformation. Straight line: linear regression of FFT points.

and the 1-site elastic selfconsistent (ELSC) model, as a function of the directional Young modulus,† for the case of axisymmetric deformation. The 1-site ELSC model is based on regarding each grain as an elastic inclusion embedded in an elastic homogeneous equivalent medium that has the average properties of the polycrystal (for details, see [17]). Consequently, the 1-site ELSC model allows the calculation of average strains inside each grain that depend only on the directional properties of the grain relative to the polycrystal. Both calculations were performed for a Cu polycrystal with 512 equiaxed, randomly oriented grains. Cu single crystals are f.c.c. and have a high elastic anisotropy (the elastic anisotropy factor of Cu is: $[c_{44} - \frac{1}{2}(c_{11} - c_{12})/c_{44}] \times 100 = 65\%$). In the FFT case, the discretization of the polycrystal is the one sketched in Fig. 1. The ELSC gives a single point per grain while the FFT gives 512 vertically aligned points per grain. As expected, the ELSC results show a monotonic behavior as a function of the directional Young modulus, with negative slopes. The FFT results show a great dispersion but, regarding the average behavior, the regression line of the whole set of FFT points also shows a negative (but less pronounced) slope. Evidently, in the n -site FFT case, the orientation still plays a role in dictating the local behavior but also the neighborhoods have a strong influence on the local response.

4. VISCOPLASTIC CASE

4.1. Formulation

In what follows, we present the solution of the local problem of an inhomogeneous viscoplastic medium undergoing an applied velocity gradient $V_{i,j}$. The resulting strain-rate and rotation-rate are given by the symmetric and skewsymmetric parts of $V_{i,j}$:

$$D_{ij} = \frac{1}{2}(V_{i,j} + V_{j,i}) \quad (15)$$

$$\Omega_{ij} = \frac{1}{2}(V_{i,j} - V_{j,i}). \quad (16)$$

If the inhomogeneous viscoplastic medium is an anisotropic polycrystal deforming by dislocation glide, its local behavior can be described in terms of a tangent approximation [18]:

$$\sigma'(\mathbf{x}) = M^{\text{tg}^{-1}}(\mathbf{x}):d(\mathbf{x}) + S^0(\mathbf{x}) \quad (17)$$

where $d(\mathbf{x})$ and $\sigma'(\mathbf{x})$ are local the strain-rate and the

† The directional Young modulus is defined as: $1/S'_{3333}$ where S'_{ijkl} is the elastic compliance tensor expressed in tensile axes, when x_3 lies along the tensile direction.

deviatoric stress, $S^o(\mathbf{x})$ is a back-extrapolated stress term and the tangent compliance modulus $M^{ig}(\mathbf{x})$ is defined by:

$$M^{ig}(\mathbf{x}) = n\dot{\gamma}_o \sum_s \frac{m^s(\mathbf{x}) \otimes m^s(\mathbf{x})}{\tau_o^s(\mathbf{x})} \left(\frac{m^s(\mathbf{x}) : \sigma'(\mathbf{x})}{\tau_o^s(\mathbf{x})} \right)^{n-1} \quad (18)$$

where the sum runs over all the potentially active slip systems(s), $m^s(\mathbf{x})$ and $\tau_o^s(\mathbf{x})$ are the symmetric Schmid tensor and the critical stress of system(s), $\dot{\gamma}_o$ is a normalization factor and n is the viscoplastic exponent (i.e. inverse of the rate-sensitivity of the material). The homogeneous reference medium can also be described in terms of a tangent behavior:

$$\Sigma' = L_o^{ig} : D + S^{oo} \quad (19)$$

where L_o^{ig} and S^{oo} are, respectively, the tangent stiffness and the back-extrapolated stress of the reference medium. Considering incompressibility, the system of differential equations to be solved in viscoplasticity becomes:

$$\begin{cases} L_{oijkl}^{ig} v_{k,lj}(\mathbf{x}) + \tau_{ij,j}(\mathbf{x}) - p_{,i}(\mathbf{x}) = 0 & \text{in RVE} \quad (20a) \\ v_{k,k}(\mathbf{x}) = 0 & \text{in RVE} \quad (20b) \\ \text{periodic boundary conditions across RVE} & (20c) \end{cases}$$

where $v_k(\mathbf{x})$ is the velocity field. The perturbation field is now defined by:

$$\tau_{ij} = \tilde{\sigma}'_{ij} - L_{oijkl}^{ig} \tilde{d}_{kl} \quad (21)$$

where $\tilde{d} = d - D$ and $\tilde{\sigma}' = \sigma' - \Sigma'$ are the local fluctuations in strain-rate and deviatoric stress, respectively. The derivation of equations (20a) and (21) is shown in Appendix A. System (20) can be also solved by means of the Green function method [26, 27], i.e.

$$L_{oijkl}^{ig} G_{km,lj}(\mathbf{x} - \mathbf{x}') + \delta_{im} \delta(\mathbf{x} - \mathbf{x}') = 0 \quad (22)$$

$$G_{km,k}(\mathbf{x} - \mathbf{x}') = 0$$

where the Green functions $H_m(\mathbf{x} - \mathbf{x}')$ and $G_{km}(\mathbf{x} - \mathbf{x}')$ are, respectively, the hydrostatic pressure and the velocity component in the x_k -direction at the point \mathbf{x}' when a unit force is applied in the x_m -direction at the point \mathbf{x}' of the RVE. The local fluctuations in the velocity and the velocity gradient fields can be obtained as convolutions in the real space:

$$\tilde{v}_k(\mathbf{x}) = \int_{R^3} G_{ki}(\mathbf{x} - \mathbf{x}') \tau_{ij}(\mathbf{x}') d\mathbf{x}' \quad (23)$$

Integrating by parts and assuming that the boundary terms vanish [24]:

$$\tilde{v}_k(\mathbf{x}) = \int_{R^3} G_{ki,j}(\mathbf{x} - \mathbf{x}') \tau_{ij}(\mathbf{x}') d\mathbf{x}' \quad (24)$$

and:

$$\tilde{v}_{i,j}(\mathbf{x}) = \int_{R^3} G_{ik,jl}(\mathbf{x} - \mathbf{x}') \tau_{kl}(\mathbf{x}') d\mathbf{x}'. \quad (25)$$

Calling $\Gamma_{ijkl} = G_{ik,jl}$ and using the convolution symbol:

$$\tilde{v}_{i,j} = \Gamma_{ijkl} * \tau_{kl}. \quad (26)$$

Transforming to Fourier space:

$$\hat{v}_{i,j} = \hat{\Gamma}_{ijkl} \hat{\tau}_{kl} \quad (27)$$

$\hat{\Gamma}_{ijkl}$ can be calculated by taking Fourier transform to (22):

$$\xi_1 \xi_j L_{oijkl}^{ig} \hat{G}_{km} - i \xi_j \hat{H}_m = \delta_{im} \quad (28)$$

$$\xi_k \hat{G}_{km} = 0.$$

Using the matrix A'_{ik} defined in (12)—replacing C_{ijkl}^o by L_{oijkl}^{ig} —system (28) can be written as [27]:

$$\underbrace{\begin{pmatrix} A'_{11} & A'_{12} & A'_{13} & \xi_1 \\ A'_{21} & A'_{22} & A'_{23} & \xi_2 \\ A'_{31} & A'_{32} & A'_{33} & \xi_3 \\ \xi_1 & \xi_2 & \xi_3 & 0 \end{pmatrix}}_{A''_{(4 \times 4)}} \times \begin{pmatrix} \hat{G}_{11} & \hat{G}_{12} & \hat{G}_{13} \\ \hat{G}_{21} & \hat{G}_{22} & \hat{G}_{23} \\ \hat{G}_{31} & \hat{G}_{32} & \hat{G}_{33} \end{pmatrix} = \begin{pmatrix} 1 & 0 & 0 \\ 0 & 1 & 0 \\ 0 & 0 & 1 \\ 0 & 0 & 0 \end{pmatrix}. \quad (29)$$

Thus:

$$\hat{G}_{jk} = A_{jk}^{\prime-1} \quad j, k = 1, 3 \quad (30)$$

$$-i \hat{H}_j = A_{4j}^{\prime-1} \quad j = 1, 3 \quad (31)$$

and:

$$V_i(\mathbf{x}) = x_i V_{i,i} \quad i = 1, 3 \quad (\text{no sum}). \quad (40)$$

$$\hat{\Gamma}_{ijkl} = -\xi_j \xi_l \hat{G}_{ik}. \quad (32)$$

As in the elastic case, $\hat{\Gamma}_{ijkl}$ can be calculated everywhere except at zero frequency (i.e. $\xi = \hat{0}$) where $\hat{v}_{i,j}$ is given directly by $\hat{v}_{i,j}|_{(\xi=0)} = 0$. With $\hat{\Gamma}_{ijkl}$ and $\hat{\tau}_{kl}$, $\hat{v}_{i,j}$ can be calculated taking inverse Fourier transform to the right term of equation (27). The fields of local fluctuation in strain-rate and rotation-rate can be readily obtained by taking symmetric and skewsymmetric parts of $\hat{v}_{i,j}$, respectively:

$$\hat{d}_{ij} = d_{ij} - D_{ij} = \frac{1}{2}(\hat{v}_{i,j} + \hat{v}_{j,i}) \quad (33)$$

$$\hat{\omega}_{ij} = \omega_{ij} - \Omega_{ij} = \frac{1}{2}(\hat{v}_{i,j} - \hat{v}_{j,i}). \quad (34)$$

The local fluctuation of the pressure field in Fourier space can be obtained as a by-product of the calculation of $\hat{\Gamma}_{ijkl}$, i.e.

$$\hat{p}(\mathbf{x}) = \int_{\mathbb{R}^3} H_{i,j}(\mathbf{x} - \mathbf{x}') \tau_{ij}(\mathbf{x}') d\mathbf{x}' = H_{i,j} * \tau_{ij}. \quad (35)$$

Hence,

$$\hat{p} = \hat{H}_{i,j} \hat{\tau}_{ij} = (-i\hat{H}_i) \xi_j \hat{\tau}_{ij} \quad (36)$$

where $-i\hat{H}_i$ is given by (31). The equilibrium statement in Fourier space is now written as:

$$\frac{\langle |\xi_s \hat{\sigma}'_{ij} - \xi_j \hat{p}| \rangle}{\|\hat{\sigma}(\xi = \hat{0})\|} < \delta. \quad (37)$$

After convergence is achieved, the velocity field in Fourier space can be obtained transforming expression (24):

$$\hat{v}_k = (-i\xi_j) \hat{G}_{ki} \hat{\tau}_{ij}. \quad (38)$$

After antitransforming the right term of equation (38) to get \hat{v}_k —with the boundary condition $\hat{v}_k|_{(\xi=0)} = 0$ —the macroscopic velocity can be calculated as:

$$v_i(\mathbf{x}) = V_i(\mathbf{x}) + \hat{v}_i(\mathbf{x}) \quad (39)$$

where $V_i(\mathbf{x})$ is the velocity field derived from the applied velocity gradient $V_{i,j}$, i.e.:

4.2. Texture and microstructure updating

After achieving convergence, the orientation and the critical stresses together with the grain morphology and the polycrystal topology should be updated. The orientation updating is performed using the local rotation-rate, given by:

$$\omega_{ij} = \Omega_{ij} + \tilde{\omega}_{ij} - \omega_{ij}^p \quad (41)$$

where Ω_{ij} and $\tilde{\omega}_{ij}$ are given by equations (16) and (34) and the plastic spin ω_{ij}^p is calculated as:

$$\omega_{ij}^p = \sum_s \alpha_{ij}^s \dot{\gamma}^s \quad (42)$$

where α_{ij}^s is the skewsymmetric Schmid tensor associated with slip system(s) and $\dot{\gamma}^s$ is the simple shear-rate in that system, given by:

$$\dot{\gamma}^s = \dot{\gamma}_0 \left(\frac{m^s(\mathbf{x}) : \sigma'(\mathbf{x})}{\tau_0^s(\mathbf{x})} \right)^n. \quad (43)$$

The critical stresses should be updated adopting a hardening law, e.g.

$$\tau_0^s = \sum_{s'} h^{ss'} \dot{\gamma}^{s'} \quad (44)$$

where $h^{ss'}$ is a hardening matrix.

The update of the grain morphology and the polycrystal topology requires the adoption of an ad-hoc criterion to reassign local properties to the Fourier points as deformation evolves. Any criterion adopted should keep the regularity of the Fourier grid at every time, in order to allow performing a new FFT calculation in the following deformation step. The criterion used in this work is as follows (see Fig. 3):

1. At time $t_1 = t_0 + \Delta t$, update the position of the initial grid $\{\mathbf{x}_d(t_0)\}$ according to: (a) the local velocity field $v_i(\mathbf{x})$ given by equations (38) and (39) and (b) the velocity field derived from the applied velocity gradient $V_i(\mathbf{x})$ given by equation (40). This gives two collections of points: the updated regular grid $\{\mathbf{x}_d(t_1)\}$ and an irregular set of points $\{\mathbf{x}(t_1)\}$.
2. Calculate $d^{ij}(t_1)$, i.e. the distance between every point $\mathbf{x}_d^j(t_1)$ and every point $x^i(t_1)$. In general, $d^{ij}(t_k)$ is defined as:

$$d^{ij}(t_k) = \text{dist}[x^i(t_k); x_d^j(t_k)]. \quad (45)$$

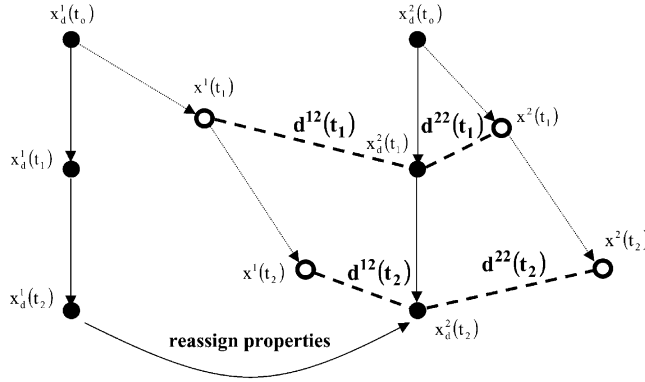


Fig. 3. Schematic representation to illustrate the morphology update procedure.

3. For each point of the regular grid $x_d^j(t_k)$, find the point of the irregular grid $x^m(t_k)$ whose distance to $x_d^j(t_k)$ is minimum, i.e. $\delta^{mj}(t_k) = \min_i [d^{ij}(t_k)]$.
4. Compute the macroscopic Von Mises equivalent strain accumulated since the latter microstructure updating:

$$\Delta E_{VM} = n^i \Delta t \sqrt{\frac{2}{3} D_{ij} D_{ij}} \quad (46)$$

where n^i is the number of deformation increments imposed to the polycrystal since the latter updating event.

5. If ΔE_{VM} is less than a threshold value (in this work we use $\Delta E_{VM} < 0.1$) perform next FFT calculation leaving the properties of $\{\mathbf{x}_d(t_1)\}$ unchanged. After achieving convergence, update $\{\mathbf{x}_d(t_1)\}$ with $V_i(\mathbf{x}_d(t_1))$. To update $\{\mathbf{x}(t_1)\}$, interpolate with the nearest values of $v_i(\mathbf{x}_d(t_1))$ to obtain $v_i(\mathbf{x}(t_1))$.
6. If ΔE_{VM} becomes greater than the threshold, proceed with the microstructure update, taking the following actions:

(a) Determine the points $x_d^j(t_k)$ of the regular grid for which $m \neq j^\dagger$ in $\delta^{mj}(t_k)$ and assign to them the properties (orientation and critical stresses) of $x_d^m(t_k)$.

(b) If $x_d^m(t_k)$ belongs to a grain g^m different from g^j , i.e. the one to which $x_d^j(t_k)$ belongs, reassign the Fourier point $x_d^j(t_k)$ to grain g^m . This change in grain belonging of the Fourier points is responsible for the grain's morphologic changes.

(c) Reset the irregular set of points to the regular grid, i.e. $\{\mathbf{x}(t_k)\} \equiv \{\mathbf{x}_d(t_k)\}$.

This updating criterion is largely based on considering that the actual coordinates of a material point (updated according to its calculated local velocity) which initially belongs to the regular Fourier grid,

will deviate smoothly from the coordinates that would result from updating them according to the homogeneous macroscopic deformation. The latter ‘‘homogeneous’’ updating of Fourier points gives rise to an evolving regular grid, which is convenient to calculate FFTs after each deformation increment.

Provided the proposed criterion involves the evaluation of minimum distances between the points of the regular grid and the points of the irregular set, the decision to reassign properties and subsequently reset the irregular set should be made when the following conditions are fulfilled: (a) a representative fraction of the grid points are ready to undergo changes in their properties; (b) if this is the case of, for instance, point P of the regular grid, the point of the irregular grid which is closest to P should have been originated from a point of regular grid which is a nearest neighbor of P. If the first condition is not fulfilled, there is risk of underestimating the morphologic evolution due to a too early reset of the irregular set of points. If the second condition does not hold, this indicates that the irregular set is heavily distorted so that its points are now too far from the regular points from where they have been originated. After testing different alternatives, we found that updating every 10% Von Mises macroscopic deformation gives sound results in the case of f.c.c. polycrystals with different configurations. In particular, the case discussed in Section 4.6, i.e. a two-phase polycrystal with a central hard region undergoing uniaxial tension, provides a benchmark for the proposed updating criterion.

4.3. Algorithm

As for the reference medium, a Voigt average (unless otherwise indicated) is assumed: $L_0^g = \langle M^{ng^{-1}}(\mathbf{x}) \rangle$. The algorithm for a single deformation increment can be initialized with $\tilde{d}^0(\mathbf{x}) = 0$ or, alternatively, using $\tilde{d}(\mathbf{x})$ corresponding to the previous increment. To get $\sigma'^o(\mathbf{x})$, invert the 5×5 non-linear system given by: $D + \tilde{d}^o(\mathbf{x}) = \gamma_0 \sum_s m^s(\mathbf{x})$

[†] This is the case, for instance, of $\delta^{12}(t_2)$ in Fig. 3, since $d^{12}(t_2)$ is the minimum distance associated with $x_d^2(t_2)$.

$\left(\frac{m^s(\mathbf{x}_d):\sigma'^o(\mathbf{x})}{\tau'_o(\mathbf{x})}\right)^n \forall \mathbf{x} \in \{\mathbf{x}_d\}$. With \tilde{d}^i, σ'^i being known, iteration $(i + 1)$ reads:

1. $\hat{\tau}'(\mathbf{x}_d) = \tilde{\sigma}'^i(\mathbf{x}_d) - L_o^{\text{vis}}:\tilde{d}^i(\mathbf{x}_d)$
2. $\hat{\sigma}'^i = \text{fft}(\sigma'^i)$ and $\hat{\tau}'^i = \text{fft}(\tau')^i$
3. For each frequency ξ , calculate \hat{G} , $-i\hat{H}$ and $\hat{\Gamma}$, according to equations (29)–(32).
4. $\hat{p}^i = (-i\hat{H}_i)\xi_j \hat{\tau}'^i_{ij}$
5. Convergence test: is equilibrium fulfilled according to (37)? If yes: calculate $\hat{v}_k = (-i\xi_j)\hat{G}_{ki}\hat{\tau}'^i_{ij}$ with $\hat{v}_{kl}(\xi = 0) = 0$ get $\tilde{v}_k = \text{fft}^{-1}(\hat{v}_k)$ update orientation, hardening and morphology (see Section 4.2) and start next deformation increment.
6. $\hat{v}_{ij}^{i+1} = \hat{\Gamma}_{ijkl}:\hat{\tau}'^i_{kl}$ with $\hat{v}_{ij}^{i+1}|_{(\xi=0)} = 0$
7. $\hat{d}^{i+1} = \text{sym}[\text{fft}^{-1}(\hat{v}_{ij}^{i+1})]$
8. Get σ'^{i+1} solving: $D + \tilde{d}^{i+1}(\mathbf{x}_d) = \gamma_o \sum_s m^s(\mathbf{x}_d)$

$\left(\frac{m^s(\mathbf{x}_d):\sigma'^{i+1}(\mathbf{x}_d)}{\tau'_o(\mathbf{x}_d)}\right)^n$ and start iteration $(i + 1)$ from step 1.

4.4. Comparison with 1-site VPSC results

As in the elastic case, we start showing a comparison between the 1-site viscoplastic selfconsistent (VPSC) model and the n -site viscoplastic FFT formulation. Figure 4 shows a comparison between the 1-site VPSC and the n -site FFT predictions of the relative longitudinal strain-rate deviation as a function of the Taylor factor (TF) for the case of axisymmetric deformation[†]. Under the 1-site VPSC assumptions, each grain is regarded as a viscoplastic inclusion embedded in an viscoplastic homogeneous equivalent medium that has the average properties of the polycrystal (for details, see [18]). Consequently, the VPSC model gives average values of the strain-rate inside each grain that depend only on the viscoplastic directional properties of the grain relative to the polycrystal. Both calculations were performed for a single-phase f.c.c. polycrystal with 512 equiaxed, randomly oriented grains deforming by $\{111\}\langle 110 \rangle$ slip. In the FFT case, the polycrystal discretization is the one sketched in Fig. 1. As in the elastic case, the VPSC gives a single point per grain while the FFT gives 512 points per grain. Unlike the elastic case, the VPSC output is not a monotonic function of TF. In fact, there are two branches at high TF that correspond to hard grains having either the $\langle 111 \rangle$ - or the $\langle 110 \rangle$ -direction near the tensile direction. However, the regression line of the VPSC points still displays a negative slope as a function of TF. As in the elastic case, the regression line of the whole set of FFT points also shows a negative but less pronounced

[†] For axisymmetric deformation along x_3 , the Taylor Factor of a grain (g) is defined as: $M^g = \sum_s \dot{\gamma}^{s:g}/D_{33}$ and gives the relative plastic hardness of a grain relative to the applied strain-rate D_{ij} .

slope, due to neighborhood effects. The overall dispersion of the local strain-rate predicted by n -site FFT formulation is twice as high as in the 1-site VPSC case.

4.5. Convergence

Using the present algorithm, the different input parameters of the viscoplastic FFT formulation affect the convergence of the model and the quality of the results. In what follows, in order to document the numerical performance of the formulation and to serve as a guide to future users, we analyze how those parameters affect the value of the left-hand term of equation (37) that gives a measure of how far the predicted local fields are from the strict fulfillment of the equilibrium condition.

4.5.1. Spatial resolution. Common sense indicates that the spatial resolution (i.e. the size of the Fourier grid that discretizes the RVE) should have an influence on the quality of the results: a more refined grid provides more degrees of freedom to adjust the local fields and reach to a better solution of the equilibrium equation. Fig. 5 shows the evolution of the error in equilibrium (EQERR) given by the left-hand term of equation (37) as a function of the number of iterations for different discretizations of the same single-phase f.c.c. polycrystal (i.e. the $8 \times 8 \times 8$ structure of 512 cubic randomly oriented grains of Fig. 1) submitted to axisymmetric deformation. The «32», «64» and «128» grids discretize each grain with 64, 512, 4096 points, respectively. As expected, EQERR diminishes as the grid becomes more refined. On the other hand, the three curves show a minimum around the 8th and the 10th iteration. After reaching that minimum, the following iterations deteriorate—rather than improve—the fulfillment of equilibrium.

Other simulation parameters that have an influence on the convergence are the rate-sensitivity and the choice of the reference medium. If the viscoplastic FFT formulation is applied to two-phase polycrystals,

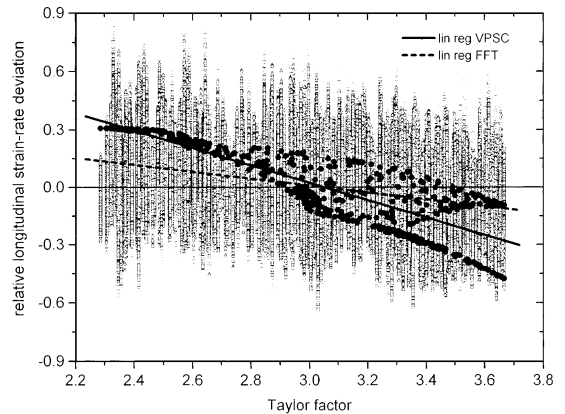


Fig. 4. Relative longitudinal strain-rate deviation calculated with 1-site VPSC and viscoplastic FFT vs. Taylor factor for a f.c.c. polycrystal under axisymmetric deformation. Straight lines: linear regression of VPSC and FFT points.

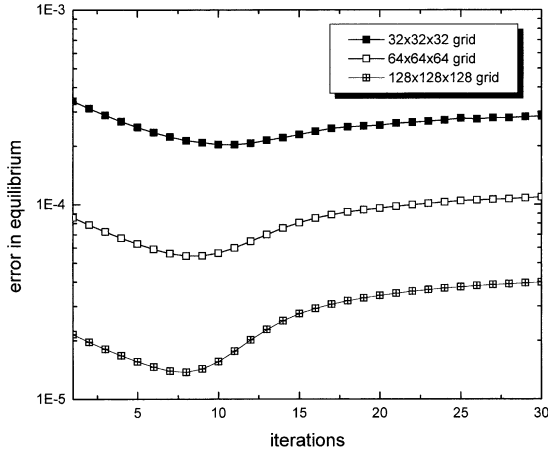


Fig. 5. Convergence of the viscoplastic FFT formulation as a function of the spatial resolution. The three cases correspond to the same polycrystal of 512 grains with: 64 ($32 \times 32 \times 32$ grid), 512 ($64 \times 64 \times 64$ grid) and 4096 ($128 \times 128 \times 128$) Fourier points per grain. The error in equilibrium is defined by equation (37).

the contrast between phases and the phase content will affect the convergence, as well. Figure 6 shows the behavior of EQERR vs. number of iterations when our model f.c.c. polycrystal of 512 grains undergoes axisymmetric deformation, for different choices of rate sensitivity, reference medium, contrast between hard and soft phases and proportion of hard phase.

4.5.2. Rate sensitivity. Figure 6(a) shows the cases of $n=10$, $n=20$ and $n=50$ for a single-phase f.c.c. polycrystal. In all cases, the reference medium corresponds to the Voigt average. Higher viscoplastic exponents increase the contrast between soft and hard grains even in a single-phase polycrystal. An interesting finding is that the value of EQERR corresponding to the first iteration remains almost unaltered. However, as n increases the minimum of EQERR occurs at a smaller number of iterations (e.g.: 2 to 4 iterations for $n=20$). For $n=50$, the equilibrium starts to deteriorate as early as in the second iteration.

4.5.3. Reference medium. Figure 6(b) shows the case of different choices for the reference medium [see equation (19)]. The Voigt and Reuss averages (derived from homogeneous strain and stress assumptions, respectively), given by: $L_o^{(Voigt)} = \langle M_o^{tg}(\mathbf{x}) \rangle$ and $L_o^{(Reuss)} = \langle M_o^{tg}(\mathbf{x})^{-1} \rangle^{-1}$ and the tangent modulus obtained with the 1-site VPSC, given by: $L_o^{(VPSC)} = \langle M_o^{tg}(\mathbf{x}); B^c(\mathbf{x}) \rangle^{-1}$ (where $B^c(\mathbf{x})$ is a localization tensor, see [18] for details) were alternatively chosen as stiffness of the reference medium. Evidently, the Voigt average appears as the only good choice while either Reuss or VPSC assumptions lead to high and oscillating EQERR values. In this case, the viscoplastic FFT formulation—due to its intrinsic non-linearity—behaves differently from the elastic FFT model which, in general, converges to the same

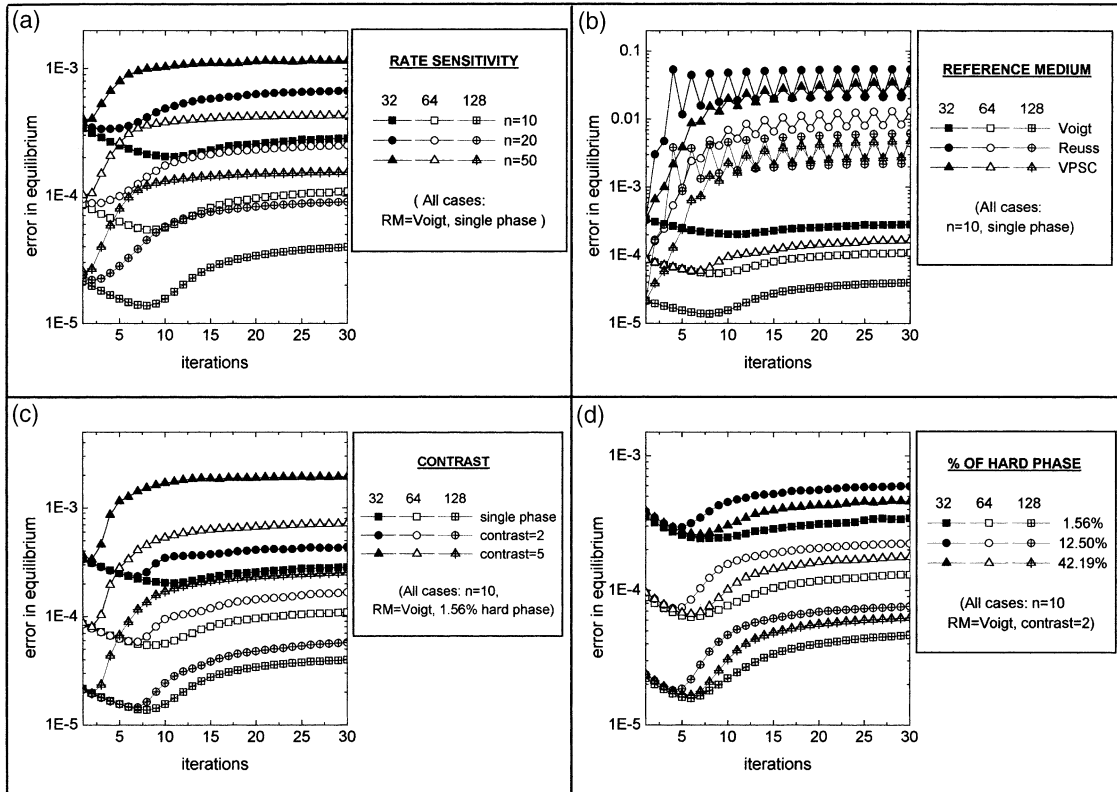


Fig. 6. Convergence of the viscoplastic FFT formulation as a function of: (a) rate sensitivity; (b) choice of reference medium; (c) contrast between hard and soft phases and (d) content of hard phase.

result for any choice of the reference medium between Voigt and Reuss, differing only in the number of iterations required [19, 20].

4.5.4. Contrast between hard and soft phases.

Figure 6(c) shows the convergence behavior for a two-phase f.c.c.-f.c.c. polycrystal for different contrasts between the hard and the soft phase. In all cases, $n = 10$ and the Voigt average is chosen as reference medium. Starting from our model polycrystal of 512 grains, a periodic two-phase polycrystal with $8/512 = 1.5625\%$ of hard phase can be constructed as shown in Fig. 7(a): a cluster of eight grains in the center of the RVE is considered to be formed by f.c.c. crystals with $\tau_0^{s(\text{hard})} = C \times \tau_0^{s(\text{soft})}$ where $\tau_0^{s(\text{hard})}$ and $\tau_0^{s(\text{soft})}$ are the critical stresses associated with the $\{111\}\langle 110 \rangle$ slip mode of the hard phase and the soft phase, respectively, and C is the contrast between the hard and the soft phase. The behavior of EQERR vs iterations for increasing contrasts is similar to the case of increasing viscoplastic exponents: the initial values of EQERR for the same resolution do not change and the minimum error is reached earlier as the contrast increases.

4.5.5. Hard phase content. Finally, Fig. 6(d) shows how the hard phase content affects the convergence. Three cases with different hard phase content of periodic f.c.c.-f.c.c. two-phase polycrystals with contrast $C = 2$ between a non-percolating hard phase and a majoritary soft phase were considered: (a) the case shown in Fig. 7(a), having 1.5625% of hard phase; (b) the case shown in Fig. 7(b), with eight evenly distributed hard clusters of eight grains each, amounting to $64/512 = 12.5\%$ of hard phase and (c) the case (not shown in the figure) of eight evenly distributed hard clusters of 27 grains each, amounting to $216/512 = 42.1875\%$ of hard phase. Compared with the cases of Fig. 6(a) and (b), for the same spatial resolution, the three curves remain closer to one another. Moreover, unlike the former cases, the

curves in Fig. 6(d) do not follow an order relative to their hard phase content (for the same resolution, the highest EQERR was obtained in the intermediate case of 12.5%). Hence, we may conclude that a higher content of hard phase does not necessarily imply an overall higher contrast in the polycrystal.

4.6. Morphology evolution

The case of a periodic two-phase f.c.c.-f.c.c. polycrystal with 1.5625% of hard phase [Fig. 7(a)] undergoing axisymmetric deformation provides an illustration on the performance of the ad-hoc criterion for morphology updating described in Section 4.2. Figure 8(a) shows the longitudinal section (the arrows indicate the loading direction) of the RVE, corresponding to layer #28 (out of 64) for the initial deformation step. The overall applied strain-rate along the longitudinal direction is 1. The right plot shows the distribution of Von Mises equivalent strain-rate with the grain boundary structure superimposed. For the sake of clarity, the grain boundary structure is separately shown in the left plot, highlighting the boundaries of the hard-phase crystals. The strain-rate distribution shows a minimum in the central hard phase and two peaks above and below the hard-phase region. It is worth recalling that the orientation of the grains where these maxima are located were randomly chosen. Therefore, those locations are not particularly softer (in a viscoplastic sense) than other regions of the polycrystal. Hence, the locations of the maxima are determined by their position relative to the hard region and not by their crystallographic orientation. This strain-rate distribution around a hard region (i.e. two maxima located along the tensile axis close to but not directly at the interphase) is the viscoplastic analogous of what Roatta *et al.* [28] found for the elastic regime at the onset of plastic deformation using an Eshelby-Mori-Tanaka approach.

Figure 8(b) shows the strain-rate distribution and the grain structure for the same section of the RVE

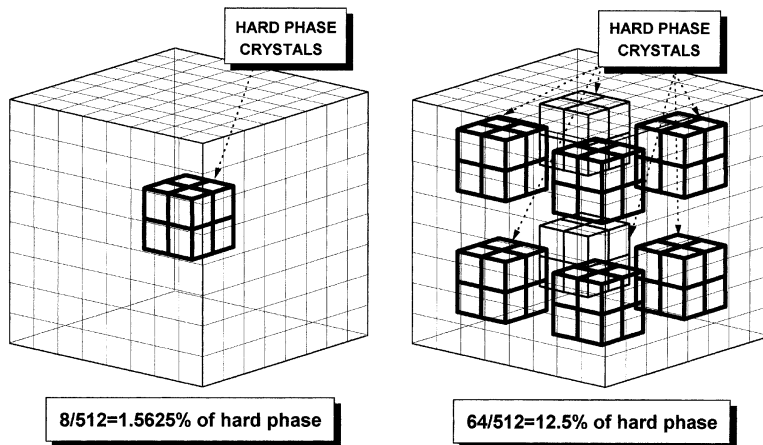


Fig. 7. Schematic representation of periodic two-phase polycrystals. The cubes drawn with thick lines are the crystals of the hard phase. (a) Case of one cluster of eight crystals. Content of hard phase = $8/512 = 1.5625\%$. (b) Case of eight clusters of eight crystals. Content of hard phase = $64/512 = 12.5\%$.

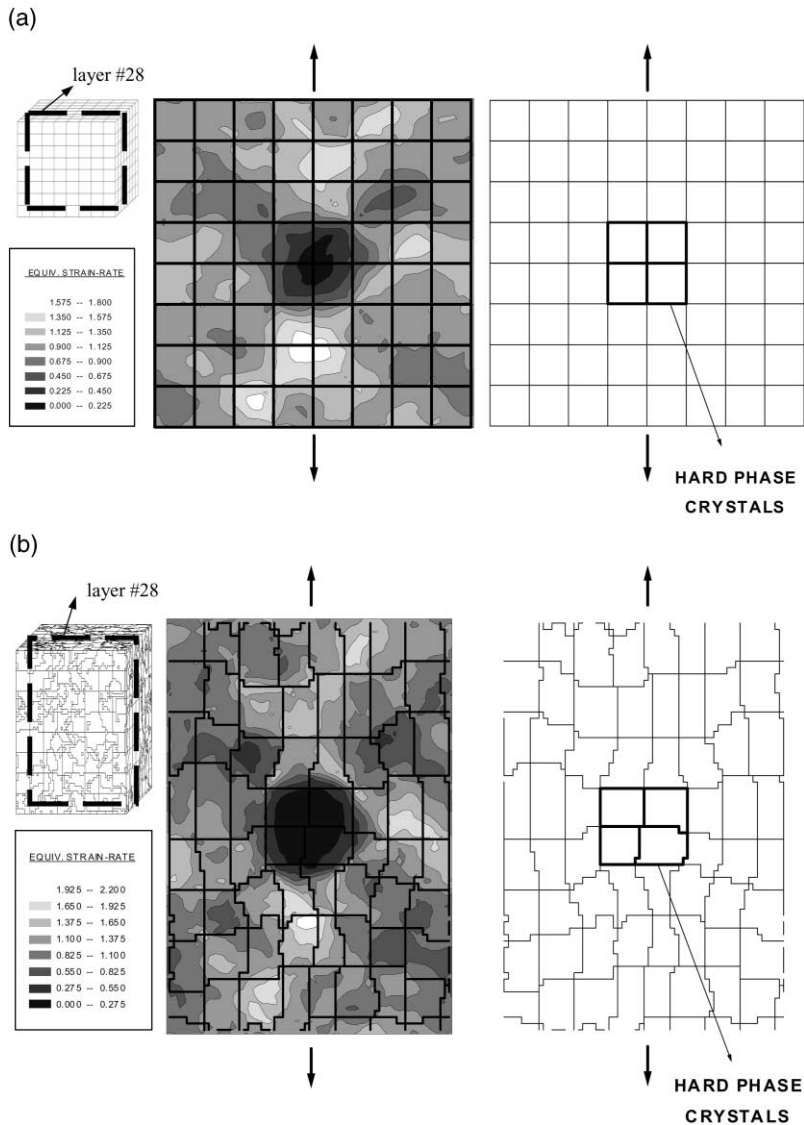


Fig. 8. Viscoplastic FFT predictions for axisymmetric deformation of a two-phase polycrystal (512 grains, $64 \times 64 \times 64$ grid, $n = 10$, $C = 2$, 1.5625% of hard phase). (a) Equivalent strain-rate and grain morphology in a longitudinal section (layer #28 of 64) corresponding to the first deformation step. (b) Equivalent strain-rate and grain morphology after 25% macroscopic strain. The hard phase crystals (thick lines) increase in width and decrease in height, relative to the whole polycrystal.

after 25% elongation (reached in 10 deformation steps of 2.5% each) with no strain-hardening [i.e. $h^{st} = 0$ in equation (44)]. The strain-rate field still shows a minimum in the central hard region while the maxima are now more disperse in the soft phase. The deformed grain-boundary structure consists of soft-phase grains which adopted a final complicated shape and hard-phase grains that essentially kept their original shape. This difference in morphology evolution between the soft-phase and the hard-phase grains reflects that the hard-phase grains remained undeformed while the soft material flowed around them, as intuitively expected from this particular configuration. As mentioned in Section 4.2, this example

provides a validation for the proposed microstructure updating criterion described in that section.

4.7. Texture development

The classical 1-site models for the prediction of texture development of polycrystals are based on the assumption of homogeneous deformation inside the grains. Under the assumptions of the simple and popular Taylor [29] Full Constraints (FC) model, the grains undergo the same strain as the whole polycrystal. As already discussed in Section 4.4, the 1-site VPSC model is less crude but still, only average states in the grains are considered. These average states depend only on the grain directional properties,

disregarding any influence from the neighbor crystals. Consequently, every material point inside the domain of a grain will undergo the same plastic distortion and, therefore, the crystallographic orientations associated with those points will go through the same changes. It follows that the crystallographic orientation will remain uniform inside the domain of each grain throughout the calculation. This determines predicted textures which are systematically sharper than the corresponding measured ones [30]. Another limitation of the classical schemes is that the actual polycrystal topology cannot be taken into account. This prevents consideration and elucidation of the role of spatial correlations in texture development. The n -site models overcome these limitations. In the following example we show how a given set of orientations can be correlated with a precise location in the polycrystal structure and how the viscoplastic FFT model predicts the development of different orientations inside a grain. Consequently, the calculated texture will be smoother than an analogous case predicted with the 1-site VPSC model.

Figure 9 shows the case of our single-phase f.c.c. model polycrystal of 512 grains submitted to plane-strain compression with no strain-hardening. Figure 9(a) displays a 3D plot of the polycrystal in its initial, undeformed state. Figure 9(c) shows a RD-ND (rolling and normal directions) section of that initial polycrystal, corresponding to layer #28 (out of 64), highlighting the boundaries of the initially equiaxed grain #94. Figure 9(b) shows the resulting 3D polycrystal after 50% thickness reduction. Figure 9(d) displays in more detail the complex grain morphology and topology in the same RD-TD section (layer #28) at the same reduction. Due to the application of the updating criterion of Section 4.2, the cross-section of grain #94 is now a complicated polygon. Figure 9(f) offers an enlarged representation of grain #94. A Fourier material point is located in the center of each rectangle in which the cross-section of the grain is subdivided. The sides of those rectangles are plotted with different line types whose thicknesses represent different misorientations between the orientations associated with two adjacent material points. In this cross section, the grain is divided by high-angle subgrain boundaries (thick interior lines) in three regions: right-most, left-most and lower central parts. A plausible interpretation of this result is that each of these regions has been influenced differently by nearest-neighbor grains. Moreover, inside each of these regions there is still some low-angle misorientation between adjacent positions. The pole figure in Fig. 6(e) is another way to represent the intragranular misorientation predicted by the model. It shows (open squares) the $\{111\}$ poles of the initial orientation of grain #94 which can be considered as a «random» orientation, i.e. far enough from any of the ideal f.c.c. rolling components. The open circles corresponds to the final orientation of grain #94 after a 1-site VPSC simulation for the same model polycrystal. It can be

seen that under 1-site VPSC that orientation is rather stable. Meanwhile, the FFT predictions (solid circles) show a large dispersion. It is worth highlighting that the 1-site VPSC prediction is *not* the average of the FFT results. This behavior predicted by the FFT model is not restricted to grains in this particular orientation. It can be generalized to grains with any orientation. We have verified (not shown here) that orientations which are less stable under the 1-site VPSC model show even more spread in the FFT case.

This development of intragranular misorientation determines lower intensities for the overall textures predicted with the FFT method compared to the 1-site models. Figure 10 shows the global textures obtained with the FFT model in the plane-strain compression case described earlier together with an analogous 1-site VPSC simulation and a typical rolling texture of copper, measured after 50% thickness reduction [31]. In all cases, the level lines represent intensities of 0.5-1.0-1.5-2.0-etc. multiples of random distribution. Qualitatively, both simulations look similar to the copper rolling texture but, comparing them quantitatively, the maximum intensity of the 1-site VPSC texture is 66% higher than the measured one. On the other hand, the FFT texture shows a peak intensity value which is very close to the measured one. However, there are still some differences between the experiment and the FFT predictions, which are essentially due to an overestimation of the brass component at early stages of texture development predicted by the model, a trend that has been reported for every formulation that deviates significantly from the Taylor FC model [32].

4.8. Numerical performance

The FFT method neither involves large matrix inversions (which are typically N^2 processes, where N is the number of points of the adopted discretization) like FEM or n -site selfconsistent models nor time-consuming integrals like the latter. Hence, the numerical performance of the FFT method (which is a $N \times \log_2 N$ process) is largely superior to small-scale FEM or n -site selfconsistent calculations for problems of the same size, at least in a single-processor machine. With the FFT approach, the interaction problem is solved by means of a one-shot procedure in Fourier space and the passage between real and Fourier spaces is performed with the highly efficient FFT algorithm. For example, a viscoplastic FFT calculation like the ones whose results are shown in Figs 8 or 9 (involving $64^3 = 262144$ material points) requires 90 s of CPU per iteration, in a 450 MHz single-processor machine. The updating scheme takes another 50 s. Therefore, the time to perform a typical deformation step consisting of eight iterations plus a final updating is: $8 \times 90 + 50 = 770$ s. Furthermore, the FFT algorithm can also be parallelized [19, 20]. In effect, for each material point, the viscoplastic constitutive law is independent from the other points of the grid (see step 6 of the algorithm described in

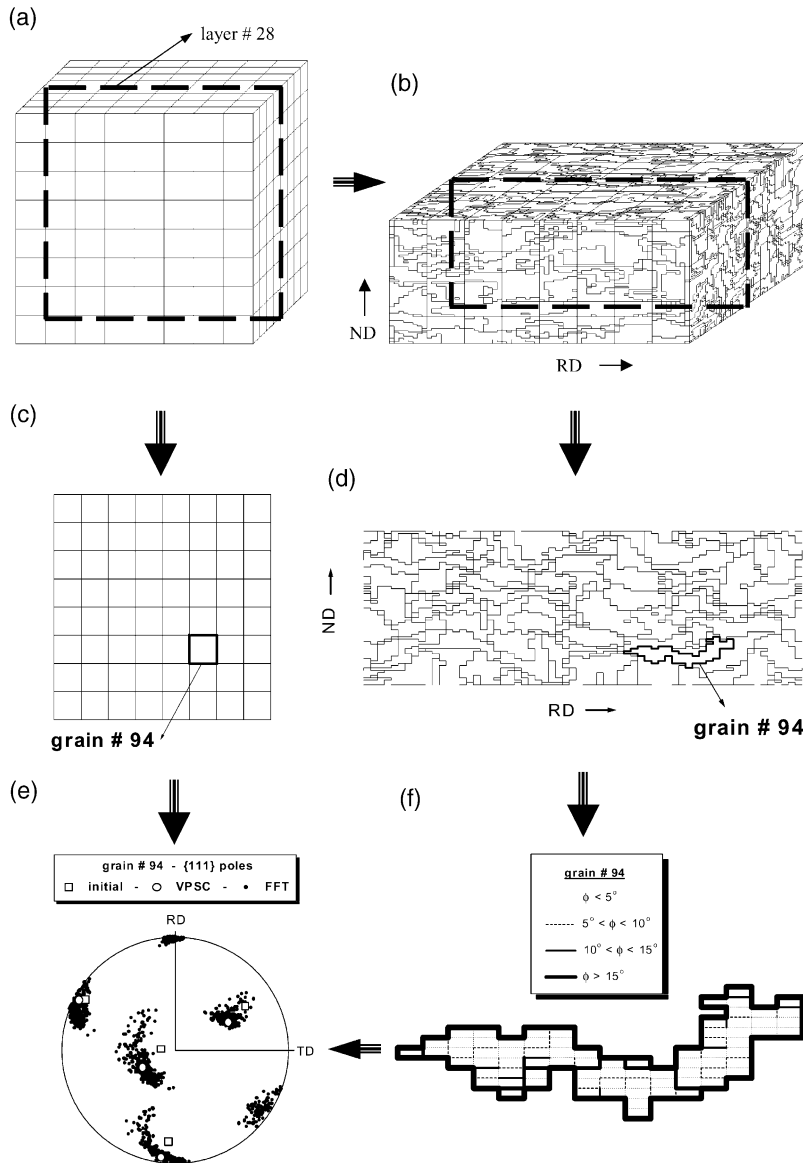


Fig. 9. Viscoplastic FFT predictions of a single-phase polycrystal (512 grains, $64 \times 64 \times 64$ grid, $n = 10$) for plane-strain compression. (a) Initial 3D polycrystal with cubic grains. (b) Deformed 3D polycrystal after 50% thickness reduction. (c)–(d) Grain morphology in a RD–ND section (layer #28 of 64) before and after deformation. (e) $\{111\}$ poles of grain #94: initial and predicted with 1-site VPSC and FFT models. (f) Morphology and intragranular misorientation ϕ of grain #94 after deformation.

Section 4.3). Moreover, the Green operators in the Fourier space ($\hat{\Gamma}_{ijkl}$, \hat{G}_{ik} and $-i\hat{H}_i$) are also local functions of each frequency ξ . Therefore, the corresponding steps of the algorithm can be parallelized. These advantages, in addition to the intrinsic optimizations of the FFT algorithm when implemented in multiple-processor computers, allow an efficient parallelization of the method.

5. CONCLUSIONS

The FFT formulation developed by Moulinec and Suquet [19, 20] has been applied to solve the local response of elastic anisotropic polycrystals and then

extended to the viscoplastic regime, including an ad-hoc criterion for microstructure updating. The numerical performance of the FFT method is largely superior to a FEM calculation for problems of the same size and, on top of that, the method can be parallelized. However, the applicability of the FFT formulation is restricted to those problems in which it is possible to identify a representative volume element and periodic boundary conditions applied to it. Otherwise, more general problems of viscoplastic deformation of heterogeneous materials would still require the use of FEM techniques.

The convergence of the viscoplastic FFT model has been analyzed with these findings: (a) fulfillment of

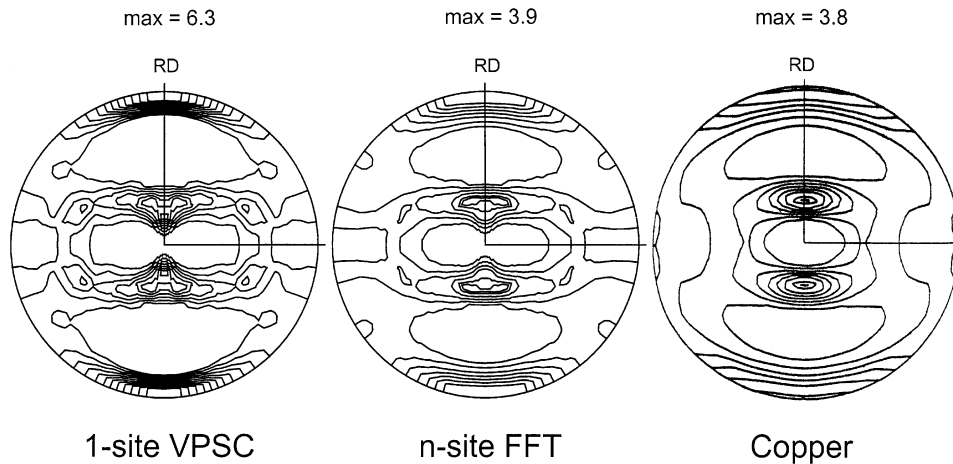


Fig. 10. Theoretical $\{111\}$ pole figures of a f.c.c. polycrystal ($n = 10$) deformed in plane-strain compression up to 50% thickness reduction predicted with the 1-site VPSC and the n -site viscoplastic FFT models and experimental $\{111\}$ pole figure of rolled copper [31] at 50% thickness reduction. Intensity lines represent 0.5–1.0–1.5–2.0–2.5, etc. multiples of random distribution.

equilibrium can always be improved by refining the Fourier grid and (b) there is an optimum number of iterations that depends on each particular problem and grid refinement. If the iterative procedure is continued beyond this optimum, the error in equilibrium starts to increase monotonically. In general, this optimum number of iterations is lower as the contrast of the local properties increases. We are aware that in order to improve the numerical performance of this formulation, further studies are needed to understand the reasons why the contrast in local properties influences in such a way the fulfillment of equilibrium, under the present algorithm.

A morphology updating scheme has been proposed. Using this scheme in combination with the FFT formulation, a sound result of grain morphology evolution has been found in the case of a two-phase f.c.c. polycrystal. The model has been also used to predict both local and overall textures of a single-phase f.c.c. polycrystal deformed in plane-strain compression. In the former case, the model allows the prediction of intragranular misorientation and subgrain formation. In the latter, the intensity of the texture predicted with the FFT model is lower than the one calculated by means of classical 1-site schemes, in good qualitatively and quantitatively agreement with typical f.c.c. textures, measured for the same reduction.

After having validated the n -site viscoplastic 3D polycrystal FFT model, we foresee several applications of this formulation to open problems in the field of micromechanical modeling, e.g. analysis of grain subdivision and subgrain formation and their role in texture development [33], calculation of intragranular distribution of stored energy and modeling of recrystallization [34], study of the role played by the spatial correlation of orientations in texture formation [35], calculation of strain heterogeneity and tex-

ture evolution in ordered [6] and random [36] two-phase aggregates, etc.

Acknowledgements—The author is grateful to Dr Pierre Suquet, Dr Pierre Gilormini and Dr Javier Signorelli for valuable discussions and to Dr Carlos Tomé and Dr Denis Solas for the use of their 3D microstructure visualization software. This work is dedicated to the memory of Dr Gilles Canova, who alerted the author about the precursor works on the FFT technique shortly before his untimely death.

REFERENCES

- Pierce, D., Asaro, R. J. and Needleman, A., *Acta Metall.*, 1982, **30**, 1087.
- Pierce, D., Asaro, R. J. and Needleman, A., *Acta metall.*, 1951, **1983**, 31.
- Brockenborough, J. R., Suresh, S. and Wienecke, H. A., *Acta metall. mater.*, 1991, **39**, 735.
- Becker, R., *Acta metall. mater.*, 1991, **39**, 1211.
- Nakamura, T. and Suresh, S., *Acta metall. mater.*, 1993, **41**, 1665.
- Bolmaro, R. E., Guerra, F. M., Kocks, U. F., Browning, R. V., Dawson, P. R., Embury, J. D. and Poole, W. J., *Acta metall. mater.*, 1893, **1993**, 41.
- Beaudoin, A. J., Mathur, K. K., Dawson, P. R. and Johnson, G. C., *Int. J. Plasticity*, 1993, **9**, 833.
- Becker, R. and Richmond, O., *Modelling Simul. Mater Sci. Eng.*, 1994, **2**, 439.
- Beaudoin, A. J., Dawson, P. R., Mathur, K. K. and Kocks, U. F., *Int. J. Plasticity*, 1995, **11**, 501.
- Becker, R. and Panchanadeeswaran, S., *Acta metall. mater.*, 1995, **43**, 2701.
- Beaudoin, A. J., Mecking, H. and Kocks, U. F., *Phil. Mag. A*, 1996, **73**, 1503.
- Sarma, G. B. and Dawson, P. R., *Acta mater.*, 1937, **1996**, 44.
- Mika, D. P. and Dawson, P. R., *Acta mater.*, 1999, **47**, 1355.
- Delaire, F., Raphanel, J. L. and Rey, C., *Acta mater.*, 2000, **48**, 1075.
- Canova, G. R., Wenk, H. R. and Molinari, A., *Acta metall. mater.*, 1992, **40**, 1519.
- Solas, D.E. and Tomé, C.N., *Int. J. Plasticity*, 2001, **17**, 737.

17. Turner, P. A. and Tomé, C. N., *Acta metall. mater.*, 1994, **42**, 4143.
18. Lebensohn, R. A. and Tomé, C. N., *Acta metall. mater.*, 1993, **41**, 2611.
19. Moulinec, H. and Suquet, P., *C.R. Acad. Sci. Paris II*, 1994, **318**, 1417.
20. Moulinec, H. and Suquet, P., *Comput. Methods Appl. Mech. Eng.*, 1998, **157**, 69.
21. Michel, J. C., Moulinec, H. and Suquet, P., *Comput. Methods Appl. Mech. Eng.*, 1999, **172**, 109.
22. Michel, J.C., Moulinec, H. and Suquet, P., *Comput. Mod. Eng. Sci.*, 2000, **1**, 79.
23. Solas, D. E., Tomé, C. N., Engler, O. and Wenk, H. R., in *Proc. 4th Int. Conf. on Recrystallization and Related Phenomena*, ed. T. Sakai and H. Suzuki. The Japan Inst. of Metals, Tokio, 1999, p. 665.
24. Mura, T., *Micromechanics of Defects in Solids*. Martinus-Nijhoff, Dordrecht, 1988.
25. Press, W. H., Flannery, B. P., Teukolsky, S. A. and Vetterliog, W. T., *Numerical Recipes*. Cambridge University Press, Cambridge, 1986.
26. Molinari, A., Canova, G. R. and Ahzi, S., *Acta metall.*, 1987, **35**, 2983.
27. Lebensohn, R. A., Turner, P. A., Signorelli, J. W., Canova, G. R. and Tomé, C. N., *Mod. Sim. Mat. Sci. Eng.*, 1998, **6**, 447.
28. Roatta, A., Turner, P. A., Bertinetti, M. A. and Bolmaro, R. E., *Mat. Sci. Eng. A*, 1997, **229**, 203.
29. Taylor, G. I., *J. Inst. Metals*, 1938, **62**, 307.
30. Kocks, U. F., Tomé, C. N. and Wenk, H. R., *Texture and Anisotropy*. Cambridge University Press, Cambridge, 1998.
31. Hirsch, J. and Lucke, K., *Acta metall.*, 1988, **36**, 2863.
32. Lebensohn, R. A. and Leffers, T., *Textures and Microstructures*, 1999, **31**, 217.
33. Hughes, D. A., Lebensohn, R. A., Wenk, H. R. and Kumar, A., *Proc. R. Soc. Lond. A*, 2000, **456**, 921.
34. Wenk, H. R., Canova, G. R., Brechet, Y. and Flandin, L., *Acta mater.*, 1997, **45**, 3283.
35. Lebensohn, R. A. and Canova, G. R., *Acta mater.*, 1997, **45**, 3687.
36. Bolmaro, R. E., Fourty, A. and Brokmeier, H. G., *Textures and Microstructures*, 1999, **33**, 125.

APPENDIX A

The local tangent viscoplastic constitutive equation is given by:

$$\sigma_{ij} = L_{ijkl}^{\text{tg}} d_{kl} + S_{kl}^{\circ} - p \delta_{ij} \quad (\text{A1})$$

where $L^{\text{tg}} = M^{\text{tg}^{-1}}$ is given by equation (18).

The local fluctuations of the tangent modulus and the back-extrapolated stress can be defined as:

$$\tilde{L}^{\text{tg}} = L^{\text{tg}} - L_0^{\text{tg}} \quad (\text{A2})$$

$$\tilde{S}^{\circ} = S^{\circ} - S^{\circ 0}. \quad (\text{A3})$$

Taking divergence to (A1) and using (A2)-(A3), the equilibrium condition reads:

$$\sigma_{ij,j} = L_{ijkl}^{\text{tg}} v_{k,lj} + S_{ij,j}^{\circ 0} + (\tilde{L}_{ijkl}^{\text{tg}} d_{kl} + \tilde{S}_{ij}^{\circ})_{,j} - p_{,i} = 0 \quad (\text{A4})$$

$$\sigma_{ij,j} = L_{ijkl}^{\text{tg}} v_{k,lj} + \tau_{ij,j} - p_{,i} = 0 \quad (\text{A5})$$

with:

$$\tau_{ij} = \tilde{L}_{ijkl}^{\text{tg}} d_{kl} + \tilde{S}_{ij}^{\circ}. \quad (\text{A6})$$

Hence:

$$\tau = (L^{\text{tg}} - L_0^{\text{tg}}):(D + \tilde{d}) + (S^{\circ} - S^{\circ 0}).$$

Rearranging terms:

$$\tau = L^{\text{tg}}:d + S^{\circ} - L_0^{\text{tg}}:D - S^{\circ 0} - L_0^{\text{tg}}:\tilde{d} = \sigma' - \Sigma' - L_0^{\text{tg}}:\tilde{d} = \tilde{\sigma}' - L_0^{\text{tg}}:\tilde{d}. \quad (\text{A7})$$